

A low-cost integrated hyperspectral imaging sensor with full temporal and spatial resolution at VIS-NIR wide range

Liheng Bian^{1,2*†}, Zhen Wang^{1†}, Yuzhe Zhang^{1†}, Yinuo Zhang¹, Chen Yang¹, Lianjie Li¹, Wen Fang^{1,2}, Jiajun Zhao¹, Chunli Zhu¹, Dezhi Zheng^{1,2} and Jun Zhang^{1*}

¹MIIT Key Laboratory of Complex-field Intelligent Sensing, Beijing Institute of Technology, Beijing 100081, China.

²Yangtze Delta Region Academy of Beijing Institute of Technology (Jiaxing), Jiaxing 314019, China.

*Corresponding author(s). E-mail(s): bian@bit.edu.cn; zhjun@bit.edu.cn;

†These authors contributed equally to this work.

Abstract

Hyperspectral imaging provides optical information with high-dimensional spatial-temporal-spectral data cubes revealing intrinsic matter characteristics. It has been widely applied in various intelligent inspection applications. The existing hyperspectral imaging systems employ individual optical prism or grating to separate different spectra, which require complicated optical design that takes a heavy load for integration. The emerging multispectral imaging sensor integrates narrow-band filters on each pixel element, wasting most light throughput and trapped in the rigorous tradeoff between spatial and spectral resolution. In this work, we report an on-chip computational hyperspectral imaging framework with full spatial and temporal resolution. By integrating different broadband filtering materials on the imaging sensor, the target spectral information is non-uniformly and intrinsically coupled on each pixel with high light throughput. Using intelligent reconstruction algorithms, multi-channel images can be recovered from each frame, realizing real-time hyperspectral imaging. Following such a framework, we for the first time fabricated a broadband (400-1700 nm) hyperspectral imaging sensor with an average light throughput of 71.8% (enabling

32.5 dB peak signal-to-noise ratio of spectral reconstruction on ColorChecker Classic chart) and 89 wavelength channels (10 nm interval within 400-1000 nm and 25 nm interval within 1000-1700 nm). The average spectral resolution achieves 2.65 nm at 400-1000 nm and 8.59 nm at 1000-1700 nm. The demonstrated spatial resolution is 2048×2048 pixels at 47 fps, with \sim 3.43 arc minute resolving ability at a 39-degree field of view. We employed the prototype sensor to collect a large-scale hyperspectral image dataset (210 scenes over 8 categories), and demonstrated the sensor's wide application potentials on a series of experiments, including chlorophyll and sugar quantification for agriculture growth, blood oxygen and water quality monitoring for human health, and face recognition for social security. The integrated hyperspectral imaging sensor is only 33.9 grams in weight without an imaging lens, and can be assembled on various resource-limited platforms such as unmanned aerial vehicles and nanosatellites, or equipped with off-the-shelf optical systems such as a microscope for direct real-time hyperspectral imaging. The technique integrates innovations from multiple fields of material, integrated circuits, computer science, and optics. It transforms the general challenge of high-dimensional imaging from one that is coupled to the physical limitations of high-cost optics manufacture and complex system design to one that is solvable through agile computation.

Keywords: hyperspectral imaging, integrated sensor, low-cost, VIS-NIR, full resolution

1 Introduction

Hyperspectral imaging captures spatial, temporal, and spectral information of the physical world, characterizing the intrinsic optical properties of each location [1]. Compared to multispectral imaging, hyperspectral imaging acquires a significantly large number of wavelength channels ranging from tens to hundreds, and maintains a superior spatial mapping capability compared to spectrometry [2]. Such great high-dimensional information enables precise distinguishment of different materials with similar colors, empowering more intelligent inspection than human vision with higher spectral resolution and wider spectral range. With such advantages, hyperspectral imaging has been widely applied in various fields such as remote sensing, machine vision, agricultural analysis, medical diagnostics, and scientific monitoring [3–8].

The most severe challenge to realizing hyperspectral imaging is how to efficiently acquire the dense spatial-spectral data cubes. Most of the existing hyperspectral imaging systems employ individual optical prism or grating elements to first separate different spectra in the spectral dimension, and then use mechanical components to scan the spatial-spectral data cube in the spatial dimensions [9]. Such a working principle is intuitive, and has led to mature market products such as AVIRIS, EnMAP, and AHSI. Such systems have been widely applied in various fields such as remote sensing (GISAT, PRISMA, and

GaoFen-5 satellites). However, this scanning mechanism requires complicated design with inevitable mechanical errors to a certain degree (especially for the cases such as distributed large arrays and vibrating platforms), and results in a long acquisition time for each frame with low temporal resolution.

As advanced by the compressive sensing theory and computational photography technique in the last decade [10], there develops a series of computational snapshot hyperspectral imaging techniques such as computed-tomography imaging system (CTIS) [11], coded aperture snapshot spectral imagers (CASSI) [12] and prism-mask multispectral video imaging system (PMVIS) [13]. The underlying foundation of such techniques lies in the intrinsic statistic that hyperspectral images exhibit strong redundancy and sparsity in different signal dimensions. The uniform working principle of these systems is first encoding multi-dimensional information into single-shot measurements, and then decoding the data cube via compressive sensing or deep learning algorithms. Although these systems effectively improve temporal resolution, they still require individual optical elements for explicit light modulation that takes a heavy load for lightweight integration [14].

Aiming for integrated hyperspectral imaging, there have been several trials for on-chip acquisition. The most intuitive routine is to extend the classic Bayer pattern of RGB color cameras by introducing more narrow-band filters, which has led commercial multispectral imaging sensors with spectrum channels ranging from 4 to 16 [15]. However, this technique suffers from a significant tradeoff between spatial and spectral resolution, and it also wastes most of light throughput for narrow-band filtering. Benefiting from finely tunable spectrum filtering ability, nano-fabricated metasurface [16–18], photonic crystal plate arrays [19], and Fabry–Pérot filters [20] have also been employed for channel selection. However, for these kinds of filters, the tuning precision is inversely proportional to spectral range. Experimentally, most of the existing prototypes cover ~ 200 nm at most in the visible range [20], with only ~ 20 channels at most. Quantum dots have also been applied for spectral modulation [21, 22], whose self-luminescence is however a challenging obstacle that degrades spectral resolution a lot. Most recently, the scattering medium has been studied for spectral encoding, which however would also introduce spatial scattering that reduces imaging resolution [23]. Besides, due to the memory effect of scattering correlation, the modulation contrast is also limited and relies only on post calibration without prior design [24]. Despite the above various on-chip techniques for spectral modulation, most of them suffer from the intrinsic tradeoff between spatial and spectral resolution, which prevents their practical applications towards high-resolution hyperspectral imaging. The detailed performance comparison is referred to Tab. 1 and Tab. S1 (see Supplementary information).

In this work, we report an on-chip computational hyperspectral imaging sensor, termed the HyperspecI sensor, with its comprehensive framework of hardware fabrication, optical calibration, and computational reconstruction. First, to effectively capture both spatial and spectral information, we

developed a broadband multispectral filter array (BMSFA) fabrication technique using photolithography. The BMSFA is composed of different broadband spectrum-modulation materials at different spatial locations. Different from the common narrow-band filters, the broadband BMSFA is able to modulate incident light at the entire spectral range, allowing much higher light throughput that benefits low-light and long-distance imaging applications. The modulated information is then intrinsically compressed and acquired by the underlying broadband monochrome image sensor, allowing for spatial-spectral compression with full temporal resolution. Second, to restore the hyperspectral data cube from the BMSFA compressed measurements, we derived a Transformer-based spectral reconstruction network (SRNet). The network consists of specially-designed spectral attention modules, enabling to compute cross-covariance across spectral channels and create attention feature maps with implicit knowledge of the spectral information and global context, which has more precise feature extraction and fuse ability than the conventional model-based reconstruction methods and convolutional neural networks. Consequently, we can reconstruct hyperspectral images with high spatial and spectral resolution from each frame, realizing real-time hyperspectral imaging.

Following the above framework, we for the first time fabricated a VIS-NIR hyperspectral imaging sensor. The spectral response range covers from 400 nm to 1700 nm, with an average light throughput of 71.8%. In low-light conditions, the HyperspecI sensor outperforms mosaic multispectral cameras and scanning hyperspectral systems, as validated in Fig. 3. The average spectral resolution achieves 2.65 nm at 400-1000 nm and 8.59 nm at 1000-1700 nm (calibrated under narrow-band monochromatic light). Experimentally, it can differentiate monochromatic light with a peak-to-peak spacing of 10 nm in the presence of multi-peak monochromatic light, as shown in Fig. 2. As for the hyperspectral imaging performance, the experiments demonstrated 89 wavelength channels with a 10 nm interval within the range of 400-1000 nm and a 25 nm interval within the range of 1000-1700 nm. The peak signal-to-noise ratio (PSNR) of spectral reconstruction achieves 32.5 dB tested on the ColorChecker Classic chart. Each channel consists of 2048×2048 pixels at a frame rate of 47 fps, maintaining ~ 3.43 arc minute optical resolving ability at a 39-degree field of view. The high frame rate allows for the capture of fast-moving objects, facilitating dynamic imaging as validated in Fig. 3. Using the USAF 1951 test chart for resolution calibration (with a 25 mm lens at an imaging distance of 30 cm), the HyperspecI sensor is able to distinguish the fourth element of the third group, where the width of the three lines is about 0.26 mm on the chart and 9 pixels in the image, resulting in a spatial resolution of 11.31 lines per millimeter.

To demonstrate the practical capabilities and wide application potentials of the HyperspecI sensor, we conducted a series of application experiments including soil plant analysis development (SPAD) and soluble solid content (SSC) evaluation for agriculture growth, blood oxygen and water quality monitoring for human health, and face recognition for social security. First, for

SPAD and SSC detection, we acquired leaf transmittance spectra and fruit reflectance spectra using the HyperspecI sensor, and established a regression model to calibrate the relationship between the spectra and the chemical components. The relative errors of the prediction dataset were only 3.73 %, indicating that the HyperspecI sensor could effectively monitor the growth state and internal quality of agricultural products. Second, leveraging the real-time imaging capability of the sensor, we conducted a blood oxygen monitoring experiment by building a specific prototype to capture the pulsatile spectral transmission of human fingertips, and demonstrated accurate blood oxygen saturation (SpO₂) diagnosis that is comparable to commercial fingertip pulse oximeters. Third, we employed the HyperspecI sensor to realize a pronounced characterization of the distribution and properties of water pollutants. The real-time imaging ability facilitates distinct segmentation of pollutant diffusion process that is however hard to observe by human eyes or common cameras. Fourth, to demonstrate the unique anti-spoofing ability of hyperspectral imaging with intrinsic material recognition, we further conducted an anti-spoofing face recognition experiment with precision higher than 95%. In comparison, the commercial face recognition product (Ding Talk, M1F) obtains only 30% accuracy in the cases of 10 silicon face masks, 10 plastic face masks, 20 print face pictures, and 10 screen display faces. Furthermore, we collected a large-scale hyperspectral image dataset employing the HyperspecI sensor, providing the first comprehensive VIS-NIR image dataset for scientific study in various fields. The dataset contains 210 hyperspectral images in total, covering 8 categories (toy, cloth, specimen, rock, plant, building, staff, and others) over both indoor and outdoor scenes.

To sum up, we report a novel on-chip computational imaging scheme for high-dimensional vision. This scheme integrates innovations from multiple fields of material, integrated circuits, computer science, optics, and so on. It transforms the general challenge of high-dimensional imaging from one that is coupled to the physical limitations of the system's optics to one that is solvable through computation. By leveraging high-cost hardware manufacture and complex system design with agile computational imaging, the remaining cost of HyperspecI sensor mainly lies on the underlying broadband sensor. As broadband imaging sensor technology is gradually matured and widely used, the cost of HyperspecI sensors would be directly decreased, making it priced competitively. This advantage is particularly significant in consumer electronic product applications, especially in mobile digital devices such as smartphones and digital cameras. What's more, such an integrated computational sensor framework can be applied to other information dimensions such as phase, polarization, and light field. We anticipate that this scheme may open a new venue for the next-generation imaging sensor of higher information dimension, imaging resolution, and integration level.

2 Principle of the HyperspecI sensor

Most conventional hyperspectral imaging devices use scanning methods to acquire three-dimensional data cubes. They suffer from bulky components and relatively long data acquisition time, thus hindering their real-time data acquisition for widespread applications. To overcome this limitation, spectral chips based on narrow-band modulations increase the number of filters on traditional color image sensors to achieve real-time multispectral imaging, which compromises the spatial-spectral resolution and sensitivity. Alternatively, compressive sensing technology enables snapshot hyperspectral imaging systems, such as CASSI, to balance spatial, spectral, and temporal resolutions in computational imaging. However, these devices still require additional spectral splitting components and have difficulty in achieving broadband full-resolution hyperspectral imaging, resulting in low universality, flexibility, and imaging accuracy.

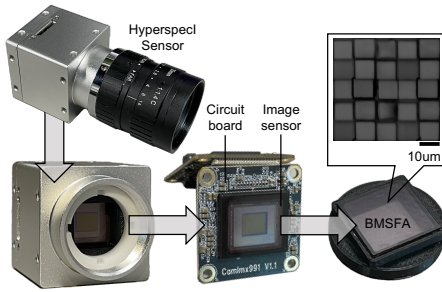
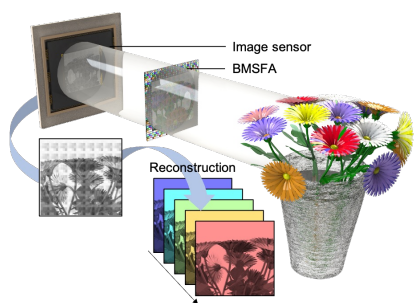
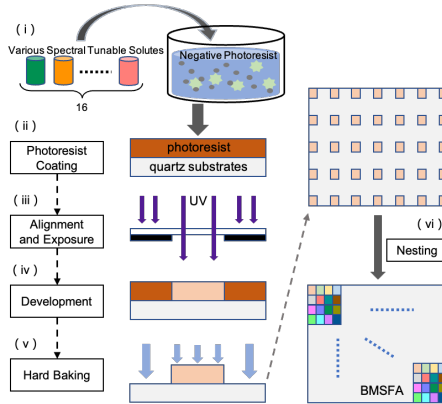
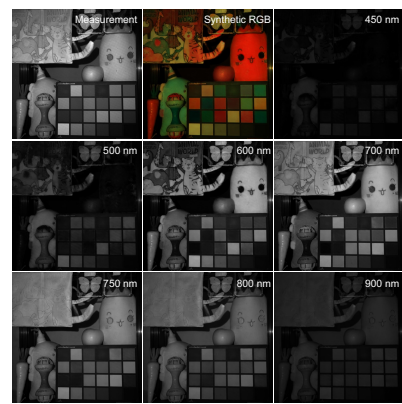
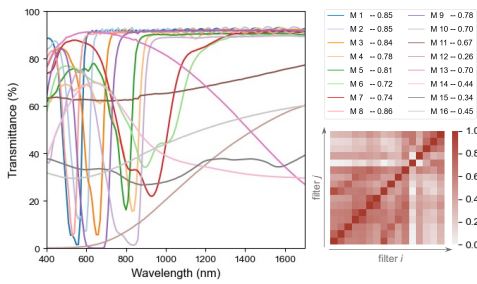
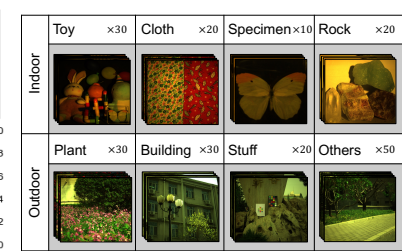
a The reported Hyperspec sensor**d** Imaging principle of the Hyperspec sensor**b** The manufacturing process of BMSFA**e** Hyperspectral imaging results**c** The transmission spectra of 16 materials on BMSFA**f** Large-scale hyperspectral image dataset

Fig. 1: Working principle of the HyperspecI sensor. **a.** The HyperspecI sensor consists of a BMSFA mask and a broadband monochrome image sensor. The BMSFA consists of a regular arrangement of 4×4 broadband materials for spectral modulation, with each filter $10 \mu\text{m}$ in size and corresponding to 2×2 image pixels. The BMSFA is cured onto the sensor surface using SU-8 photoresist. **b.** The manufacturing process of BMSFA. We developed a low-cost fabrication strategy to produce BMSFA using photolithography. (i) Sixteen pre-selected and prepared broadband modulation materials were mixed thoroughly with negative photoresist to form the broadband spectrum modulation material. (ii) The material was spin-coated onto the quartz substrate. (iii) The wafer was aligned with the designed 4×4 unit mask and exposed, followed by (iv) development and rinsing. (v) The broadband modulation material was hardened into $10 \mu\text{m}$ square structures on the substrate through a hard baking process. (vi) The remaining 15 materials were sequentially patterned through nesting to obtain the final BMSFA mask with a $10 \mu\text{m}$ resolution. **c.** The transmission response of the 16 materials, average light throughput of each material, and correlation coefficients matrix between each spectral response. The larger throughput ensures lower measurement noise, and the smaller correlation ensures a more random sampling. **d.** The imaging principle of the HyperspecI sensor. The light emitted from the target scene is encoded in the spectral dimension after passing through BMSFA, and then captured by the broadband image sensor. The collected two-dimensional compressed data is then processed by a well-trained neural network to decouple and output hyperspectral images. **e.** The imaging results and details of the target scene were taken by the HyperspecI sensor. **f.** Illustration of the collected large-scale hyperspectral image dataset using the HyperspecI sensor.

In order to address these issues, we propose an on-chip-modulated hyperspectral imaging sensor, termed HyperspecI sensor, which has a wide spectral range and full spatial and spectral resolution. The sensor consists of two main components: a broadband multispectral filter array (BMSFA) and a monochrome image sensor (Fig. 1a). The BMSFA encodes the high-dimensional hyperspectral data cube of the scene, and the imaging sensor acquires the coupled two-dimensional measurements compressed along the spectral dimension. Through a physical model and data-driven joint driving method, the high-precision hyperspectral data could be reconstructed with high probability from the measurements (Fig. 1d and Supplementary Section 6 for specific reconstruction algorithms).

In the preparation of BMSFA, we used photoresist, a byproduct of conventional photolithography, as the modulation material to produce the photoresist solution (see Supplementary Section 2) that exhibits different spectral modulation. The solution was used for photolithography to leave micron-sized square structures on a quartz substrate, forming a broadband material array. Repeated photolithography steps (SUSS MA-6) produced multiple layers of patterned structures, resulting in the final BMSFA, as shown in Fig. 1b. To

meet the demands for different spectral imaging ranges, we designed and prepared BMSFAs with different material systems and spatial arrangements. We integrated them with CMOS and InGaAs image sensors separately (see Supplementary Section 4), thus achieving spatial resolutions of 2048×2048 pixels and spectral resolutions of 2.65 nm in the range of 400-1000 nm and a spectral resolution of 8.59 nm in the range of 400-1700 nm. The hyperspectral sensor can replace traditional spectral cameras for spectral measurement and imaging in various scenarios. A prototype camera with the integrated chip is shown in Fig. 1a and was used in subsequent experiments in this paper.

The full-resolution hyperspectral imaging capability achieved by our sensor is mainly attributed to encoding the target scene's light by BMSFAs in both spatial and spectral dimensions. Based on the prior assumptions of spatial sparsity and spectral similarity in the measured hyperspectral data, a neural network model was used to perform the spectral reconstruction. Although the solution is underdetermined, the incoherence of the measurement matrix ensures that the network model can reconstruct high-quality hyperspectral images with high probability and low error. Moreover, the weak correlation between filter responses ensures the compressive performance and reconstruction accuracy of the target scene. For example, using the 400-1700 nm BMSFA, Fig. 1c shows the transmission spectra and correlation matrix based on the 16 modulation material filters. In addition, the area under the transmission spectral curve of the filters in Fig. 1c determines the average light throughput of the array, which is critical for achieving high sensitivity and low measurement noise.

To evaluate the sensor's imaging performance, we obtained the hyperspectral images of complex scenes under a broadband spectral light source in the laboratory. The imaging results (Fig. 1e) demonstrate that the HyperspecI sensor can capture rich spatial details and maintain high spectral accuracy across a broad spectral wavelength range.

3 Performance of the HyperspecI sensor

We conducted various experiments to assess the performance of our HyperspecI sensor in both spatial and spectral dimensions. To reconstruct hyperspectral images from the measurement data obtained by the HyperspecI sensor, we proposed a deep learning method SRNet (see Supplementary Section 6 for details). As shown in Fig. 2a, the reconstructed hyperspectral images were visualized in RGB format using the 1931 CIE color-matching function. We also compared the reconstructed spectra with ground truths collected by commercial spectrometers at the positions indicated by yellow markers in the RGB images. In addition, we quantitatively evaluated the reconstruction errors of the spectra using a standard color calibration chart (ColorChecker Classic) under average laboratory lighting with 405 lux (Thorlabs, SLS302). The average PSNR of reconstructing results for 24 colors was found to be 32.5 dB (see Supplementary Fig. S15 for details).

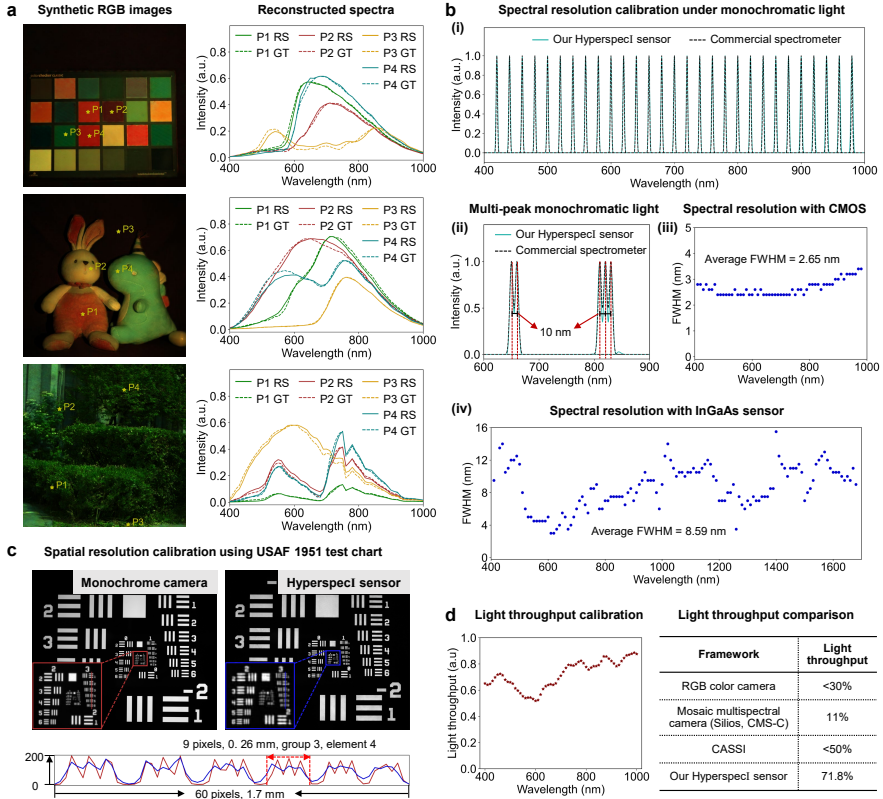


Fig. 2: Hyperspectral imaging performance of the HyperspecI sensor. **a.** Hyperspectral imaging results of real-world scenes. Reconstructed hyperspectral images were visualized in synthetic RGB form on the left. The spectral comparison between reconstructed spectra (RS) and ground truth (GT, acquired by the commercial spectrometers of Ocean Optics USB 2000+ and NIR-Quest 512) were represented on the right (denoted by solid and dashed lines). **b.** Spectral resolution calibration. (i-ii) Spectral comparison of HyperspecI sensor (green solid lines) and the commercial spectrometer (black dashed lines). The narrow-band monochrome light was generated by the commercial monochromator of Omno151. (iii-iv) The full width at half maximum (FWHM) of each band was measured under monochromatic light with 10 nm intervals. When the HyperspecI sensor was integrated using a CMOS image sensor (Sony IMX264), the average spectral resolution was found to be 2.65 nm. Similarly, when it was integrated using an InGaAs image sensor (Sony IMX990), the average spectral resolution was measured to be 8.59 nm. **c.** Spatial resolution calibration using the USAF 1951 resolution test chart. The curves of a monochrome camera (red line) and our sensor (blue line) for elements 1-6 of group 3 were presented. **d.** Light throughput calibration. The average light throughput reaches 71.8%, which is much higher than that of other imaging devices such as RGB cameras (<30%), mosaic multispectral cameras (11%, Silios, CMS-C), and coded aperture snapshot spectral imagers (CASSI) (<50%).

We presented reconstruction results of monochromatic light from 400 to 1000 nm with an interval of 0.2 nm, as illustrated in Fig. 2b. According to compressive sensing theory, narrow-band light can be reconstructed with higher quality due to its sparsity. In Fig. 2b (i), we compared the reconstruction results of our sensor and commercial spectrometer under single-peak monochromatic light. To evaluate the sensor's performance under more complex scenarios, Fig. 2b (ii) illustrates the reconstruction performance for multi-peak monochromatic light, indicating that HyperspecI sensor can distinguish monochromatic light with a peak-to-peak spacing of 10 nm. The average spectral resolution of our sensor is 2.65 nm using a CMOS image sensor for imaging, as shown in Fig. 2b (iii), which is determined by the full width at half maximum (FWHM) of the reconstructed spectra of monochromatic light. We also displayed the FWHM of each band under monochrome light in Fig. 2b (iv). On the other hand, when HyperspecI sensor is integrated with an InGaAs image sensor, the average spectral resolution is 8.59 nm.

To evaluate the spatial resolution, we captured images of the USAF 1951 spatial resolution test chart using a monochrome camera (Sony IMX264) and our HyperspecI sensor respectively, as illustrated in Fig. 2c. Analysis of the resolution chart images reveals that our sensor is able to distinguish the third group and the fourth element, where the width of the three lines is about 0.26 mm on the chart or 9 pixels in the image, resulting in a spatial resolution of 11.31 lines per millimeter. Furthermore, our comparison results demonstrate

that our sensor's spatial resolution is comparable to that of the commercial monochrome camera, indicating that our sensor achieves full-resolution hyperspectral imaging.

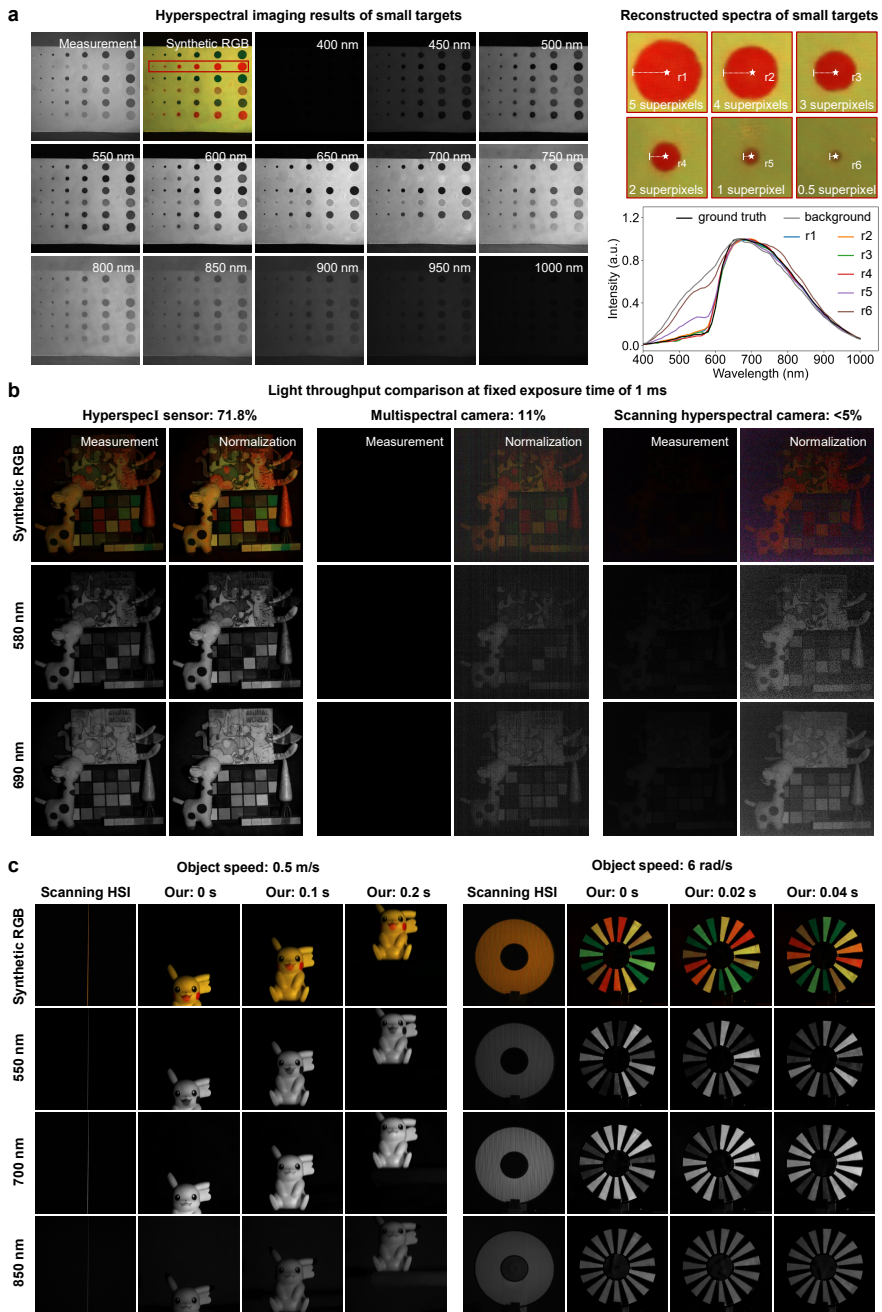


Fig. 3: Hyperspectral imaging performance comparison among different products. **a.** Hyperspectral imaging results of small targets. On the left, we displayed the measurements, the synthetic RGB images, and spectral images of several exemplar bands. On the right, the comparison is shown among the background spectrum, ground truth, and reconstructed spectra of the small targets, which were marked in the synthetic RGB image with a red rectangle. **b.** Hyperspectral imaging comparison in low-light conditions. The imaging results of our HyperspecI sensor, mosaic multispectral camera, and scanning hyperspectral imaging camera were compared at a fixed exposure time of 1 ms. We presented synthetic RGB images and spectral images (at 580 nm and 690 nm) of the measurements, along with the corresponding normalized data. **c.** Hyperspectral imaging results at video frame rate. On the left, we presented the results at three different time points (0 s, 1 s, and 2 s) while the object was undergoing translational motion at a speed of ~ 0.5 m/s. On the right, we presented the results at three different time points (0 s, 0.02 s, and 0.04 s) while the object was undergoing rotational motion at a speed of ~ 6 rad/s. We also compared these results with those obtained using a scanning hyperspectral imaging (HSI) camera. The reconstructed results were demonstrated using synthetic RGB images and spectral images at 550 nm, 700 nm, and 850 nm.

In addition, the demonstrated spatial resolution is 2048×2048 pixels at a rate of 47 fps, with a resolving ability of approximately 3.43 arc minutes for a 39-degree field of view. The light throughput across different spectral ranges is depicted in Fig. 2d, which illustrates that the average sensitivity of our HyperspecI sensor is 71.8%. The value is much higher than that of RGB color cameras, mosaic multispectral cameras, and CASSI.

When detection targets are relatively small, the detection accuracy can be affected by background information and environmental noise. Therefore, it is essential to confirm the spectral reconstruction performance of the sensor for small targets. To achieve this, we conducted experiments on a series of point targets with varying sizes, as illustrated in Fig. 3a. The results indicate that HyperspecI sensor exhibits better spectral reconstruction accuracy when the radius of small targets is greater than a superpixel. The superpixel represents the smallest components of spectral modulation structure consisting of 4×4 material points or 12×12 pixels in the imaging sensor.

As shown in Fig. 3b, we compared the hyperspectral imaging performance of HyperspecI sensor, the mosaic multispectral camera (Silios, CMS-C), and a scanning hyperspectral camera (FigSpec, FS-23) in low-light conditions. The experimental setup utilized the laboratory light source (Thorlabs, SLS302) with an illuminance level of 290 lux. The exposure time for all these devices was set to 1 ms. However, the scanning hyperspectral camera takes approximately 30 seconds to complete the scanning process and capture a hyperspectral image. Experimental results demonstrate that our sensor, with its higher light throughput and superior signal-to-noise ratio, is better suited for imaging in

low-light scenes. As shown in Fig. 3c, our sensor performs hyperspectral imaging of moving objects at a frame rate of 47 fps. We validated the imaging performance under translational motion at a speed of 0.5 m/s and rotational motion at a speed of 6 rad/s. The results prove that our sensor achieves full temporal resolution dynamic imaging at a high frame rate, while traditional scanning hyperspectral cameras are unable to capture dynamic scenes.

The above experiments have demonstrated that our sensor possesses high spatial-spectral resolution in a broad spectral range, and is also suitable for applications such as small target detection, low-light and dynamic scene hyperspectral imaging.

4 Application of HyperspecI sensor for intelligent agriculture

Effective detection of target components is imperative to improve crop management strategies, such as fertilization, irrigation, and harvest optimization. The SPAD index, which is highly correlated with the chlorophyll content of leaves [25], plays a fundamental role in assessing the physiological status of plants. Similarly, SSC is an important indicator for evaluating fruit quality and determining the optimal time for harvesting. However, conventional SPAD and SSC measurements involve destructive sampling, which is complicated and time-consuming. With the advancements in molecular spectroscopy analytical technology combined with chemometric methods, VIS-NIR spectroscopy analysis, which characterizes target components, has become a widely used non-destructive alternative for evaluating internal qualities. In order to further validate the performance of the reported HyperspecI sensor, a specific prototype was developed for transmissive and reflective spectra acquisition (as shown in Fig. 4a). Meanwhile, non-destructive experiments were conducted to measure SPAD and SSC, respectively.

Fig. 4b illustrates the principle behind SPAD detection based on the Lambert-Beer law, which describes the correlation between the intensity of light absorption of leaves at a particular wavelength and the chlorophyll concentration. For this study, HyperspecI sensor was used to obtain transmission spectra of 200 selected leaves. Subsequently, the characteristic peaks at 660 nm (chlorophyll absorption peak) [26] and 720 nm (only related to leaf thickness and used as a variable control) were chosen as inputs, while SPAD was measured using a commercial chlorophyll meter as output to establish a regression model. To validate the model's performance, an additional set of 20 different leaves was collected for testing purposes. The comparison between the measured and true values is shown in Fig. 4e, with a root mean square error (RMSE) of 1.0532 for the test set.

The experimental procedure of non-destructive detection of SSC in apples is described in Fig. 4c. The left side of the figure displays the hyperspectral imaging system, while the right side depicts the procedure of quantitative model establishment and evaluation. As shown in Fig. 4f, the spectral curves exhibit

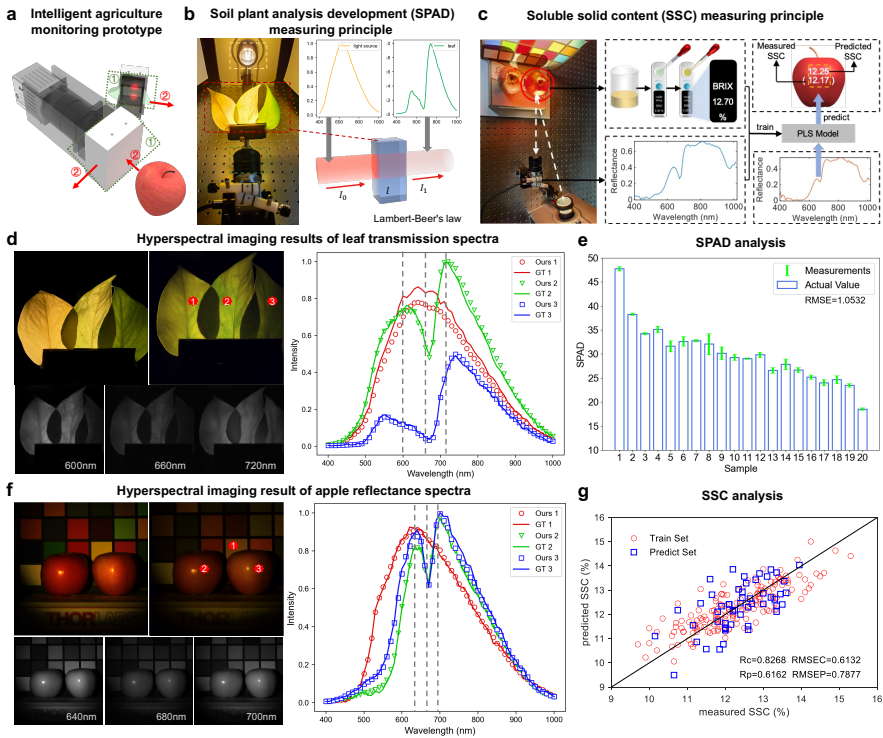


Fig. 4: Application of the HyperspecI sensor for intelligent agriculture. **a.** We built a prototype using HyperspecI sensor for the acquisition of spectra, including two distinct modes: leaf transmission spectra acquisition mode and apple reflectance spectra acquisition mode. **b.** The working principle of measuring soil plant analysis development (SPAD) index, which is used to evaluate the chlorophyll content of leaves. **c.** The working principle of measuring soluble solid content (SSC), which is used to evaluate apple quality. **d.** Captured leaf images using an RGB camera (top left) and reconstructed hyperspectral images using HyperspecI sensor (top right, shown in synthetic RGB form). The right subgraph shows a comparison between the spectra acquired by a commercial spectrometer and reconstructed spectra at three randomly selected locations. **e.** SPAD evaluation results using the reconstructed spectra of HyperspecI sensor. **f.** Captured apple images by an RGB camera (top left) and reconstructed hyperspectral images by the HyperspecI sensor (top right, shown in RGB form). The right subgraph shows a comparison between the spectra acquired by a commercial spectrometer and reconstructed spectra at three randomly selected locations. **g.** Measured SSC using a commercial product versus predicted SSC using the partial least squares (PLS) regression with respect to the solid 1:1 line.

prominent absorption peaks near 640 nm and 700 nm, as well as a trough near 680 nm. The peak at 640 nm is primarily related to the color of the apple's epidermis, while the trough near 680 nm is influenced by chlorophyll reflectance, and the peak near 700 nm is associated with octave stretching vibrations of C-H and O-H bonds. These characteristics highlight the potential of HyperspecI sensor for analyzing SSC distribution in apples. Partial least squares regression was utilized to extract potential information from complex spectra. Fig. 4g is the scatter plot of measured and predicted SSC, where points closer to the solid line indicate better model performance. The correction coefficient and RMSE were found to be 0.8264 and 0.6132% for the training set, and 0.6162 and 0.7877% for the test set, respectively. These results underscore the significant potential of HyperspecI sensors for intelligent agriculture applications (see Supplementary Section 8 for more details).

5 Application of the HyperspecI sensor in real-time health monitoring

In recent years, health issues have garnered increasing attention, leading to the proliferation of health testing equipment. This includes devices for monitoring blood oxygen saturation and assessing water quality, among others. However, conventional methods for oxygen saturation monitoring and water quality testing often involve large equipment and complex processes, impeding real-time and lightweight detection. Overcoming this challenge is crucial to enable prompt and convenient testing. Fortunately, advancements in spectral technology have facilitated the development of compact devices for oxygen saturation monitoring and water quality testing. Leveraging the capabilities of spectral technology, the feasibility of HyperspecI sensors for real-time rapid health testing applications has been experimentally verified.

To enable blood oxygen saturation monitoring, we have developed a device based on spectroscopy, as shown in Fig. 4a. This method relies on detecting changes in arterial blood absorption at specific wavelengths due to pulsation. First, the finger to be measured is placed into the device, and HyperspecI sensor acquires the transmission spectra of the finger using a broad-spectrum light source for a period of time at a collection rate of 100 Hz. Then the acquired time series images are processed to obtain a series of spectral profiles at a single location on the finger. Finally, the pulsatile component (AC) is extracted from the photoplethysmography signal at two characteristic bands (780 nm, 830 nm). The blood oxygen saturation can be obtained using the formula (see Supplementary Section 9 for details). Comparative results between the HyperspecI sensor and a commercial oximeter are shown in Fig. 4b.

To further validate the dynamic spectral imaging accuracy of HyperspecI sensor and explore its capability in water quality detection, we simulated the process of effluent diffusion. Accurate real-time monitoring is essential for water quality testing. In our experiment, we prepared two solutions with similar colors but different components: standard magenta dye solution #2 and

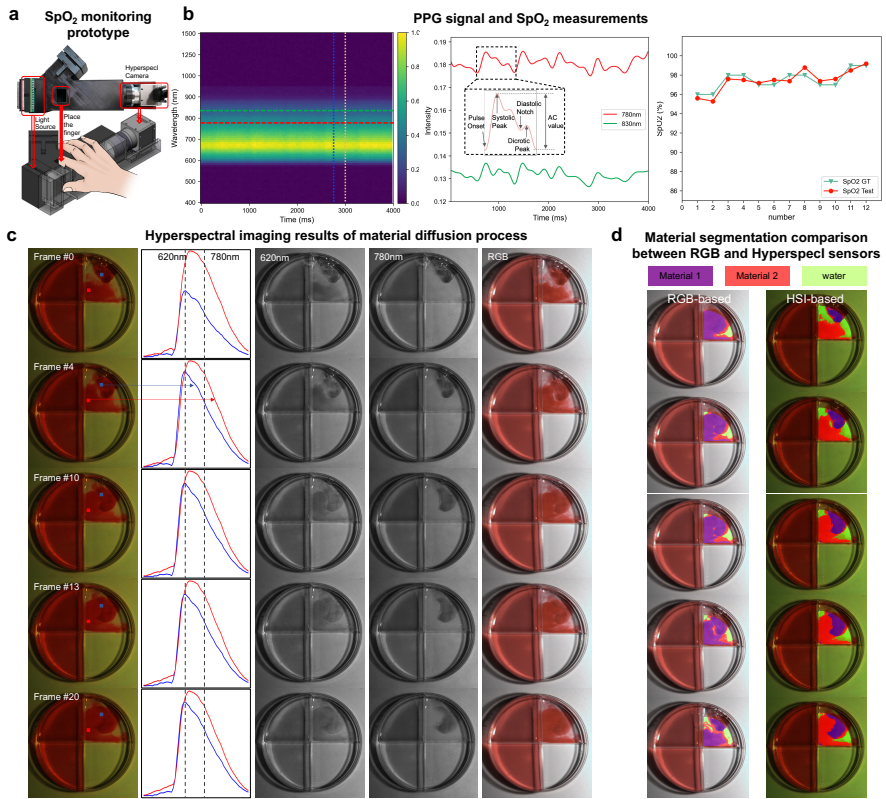


Fig. 5: Application of the HyperspecI sensor for blood oxygen and water quality monitoring. **a.** The prototype we built using HyperspecI sensor for blood oxygen saturation (SpO₂) monitoring. **b.** The transmission spectra through the finger obtained over a period of time at a collection rate of 100 Hz. The figure displays two photoplethysmography (PPG) signals at 780 nm and 830 nm, corresponding to two bands with different intensities of HbO₂ and Hb absorption. The blood oxygen saturation of the measured sample can be accurately determined by analyzing and calibrating the PPG signals at two characteristic bands. Comparative analysis with a commercial oximeter demonstrates a high level of consistency and agreement in the obtained results. **c.** Five frames of HyperspecI measurements demonstrating the diffusion process, accompanied by corresponding images captured using an RGB camera. In the petri dish, solution #1 was positioned in the upper left corner, and solution #2 was placed in the lower left corner. These two solutions were added to distilled water in the upper right corner. Hyperspectral images acquired by HyperspecI sensor are presented in RGB format. **d.** Comparison of segmentation masks between an RGB camera (left) and HyperspecI sensor (right).

the same concentration of magenta dye with infrared absorption material solution #1 (in a 20:1 ratio). These two solutions were rapidly injected into the distilled water (as shown in the upper right corner of the petri dish) and diffused freely. Meanwhile, the diffusion process was recorded using HyperspecI sensor and RGB camera. As shown in Fig. 4c, the captured images from RGB camera are difficult to distinguish between the two solutions. However, when we selected the spectral curves of the two solutions from the frames captured by HyperspecI sensor, apparent differences were observed. To further illustrate the distribution of the two solutions, Fig. 4c also shows the imaging results in the 620 nm and 780 nm, due to significant absorption around 800 nm of solution #2. Furthermore, machine learning-based image segmentation algorithms were employed to segment the frames captured by the RGB camera and HyperspecI sensor (Fig. 4d). The segmentation of the RGB images primarily relied on morphological segmentation and color information, while the segmentation of hyperspectral images was based on spectral information. Due to the nearly consistent response of the two solutions in the visible light range, the diffusion process of the solutions was difficult to observe in RGB images. However, segmentation results of the hyperspectral images exhibited clearer boundaries and accurately illustrated the location and physical diffusion process of the solutions. Therefore, HyperspecI sensor, with its high spectral accuracy and high frame rate, holds great potential for a wide range of high-precision dynamic monitoring applications.

6 Application of HyperspecI sensor for face anti-spoofing

Facial recognition, as a vital technology in biometric identification, has found widespread applications in security domains such as access control, electronic payments, and so on. However, existing facial recognition methods primarily focus on the morphological features of the face and are susceptible to attacks from realistic spoofing faces, such as 3D-printed masks made of various materials. Spectral detection is a method of distinguishing different substances by their spectra, even when they share the same form and color. Moreover, existing research and extensive experiments in this work have revealed significant differences in spectral data between real and various fake faces, which can be used for face anti-spoofing (FAS). Based on the HyperspecI sensor, real-time face detection and anti-spoofing recognition can be achieved simultaneously at high frame rates.

With the excellent spectral imaging precision and speed of HyperspecI sensor, we are able to directly integrate it into existing face recognition frameworks, thereby replacing the traditional RGB cameras that expand the dimensions and information content of data acquisition. The proposed anti-spoofing face recognition pipeline based on the HyperspecI sensor is illustrated in Fig. 6a. Initially, the acquired spectral images from the HyperspecI sensor are synthesized into RGB images, which serve as input for conventional face

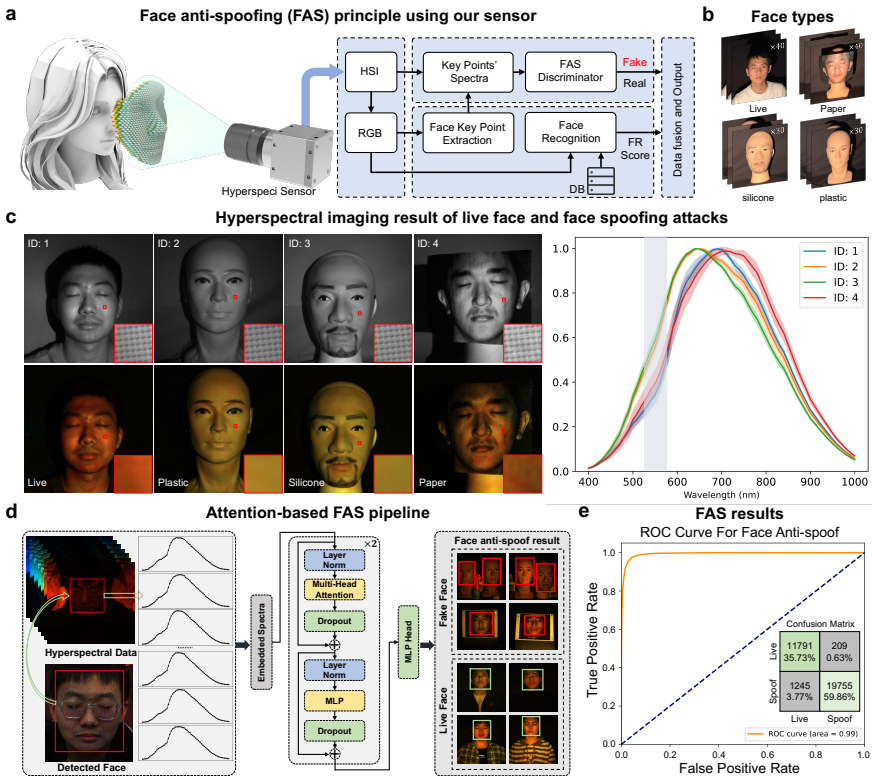


Fig. 6: **a.** The face recognition system using HyperspecI sensor for face anti-spoofing (FAS). **b.** The face dataset we collected is composed of different types, including live faces, paper-printed faces, silicone faces, and plastic faces. **c.** Imaging results of different faces using HyperspecI sensor. The left subgraph presents the imaging results and corresponding synthetic RGB images, while the right subgraph shows the spectral curves of the same location, revealing spectral differences among different face materials. **d.** The attention-based FAS pipeline, which is composed of several phases, including using the key locations of the face extracted from the synthetic RGB image to locate the spectral curve at the corresponding positions in the hyperspectral image, inputting the spectral data into the neural network, performing feature extraction through the two-layer Transformer encoder and the MLP layer to map the feature to spoofing discrimination results. **e.** Experiment results of HyperspecI sensor-based FAS. The area under the curve (AUC) values of receiver operating characteristic (ROC) curves achieves over 99%, showing superior performance in distinguishing different materials.

keypoint detection and recognition algorithms, resulting in face recognition outcomes. Simultaneously, facial spectral data is extracted from the measurement using face keypoints as input for attack detection, resulting in detection outcomes. The final face anti-spoofing recognition results are obtained by fusing the results from the two parallel algorithms. To validate the effectiveness and reliability of spectral face recognition, we constructed a face dataset encompassing various types of spoofing attacks, including silicone masks, plastic faces, and paper masks. This dataset comprises facial data with diverse appearances, capture angles, and disguise types, as depicted in Fig. 6b.

We conducted extensive testing on the reflectance spectra of faces with different materials. As shown in Fig. 6c, live faces exhibit stronger absorption in the range of 500-600 nm (the absorption peak of hemoglobin). Furthermore, faces within the same category display consistent spectral distributions. These findings provide strong evidence and a foundation for implementing spectroscopy-based anti-spoofing methods in facial recognition. Using the above method, collect face images using HyperspecI camera to construct spectra data to train the FAS model shown in Fig. 6d. Remarkably, using only spectral dimension information, we achieve 95.59% accuracy in real testing scenarios. In the context of daily-life face recognition devices, the substitution of the acquisition device with HyperspecI allows for enhanced face anti-spoofing recognition while keeping the face recognition algorithm intact. This integration merely requires the inclusion of a straightforward FAS algorithm, ensuring recognition performance and enabling a safer anti-spoofing capability. Further details regarding the implementation and algorithm for FAS are shown in Supplementary Section 10.

7 Conclusion and Discussion

This work introduces a novel hyperspectral imaging sensor, the HyperspecI sensor, which acquires encoded hyperspectral information by combining a BMSFA and a monochrome. The BMSFA is the primary component of our sensor, which incorporates diverse broadband spectrum-modulation materials at various spatial positions. We fabricated the BMSFA by dissolving 16 materials in photoresist and performing precise ultraviolet photolithography processes in 16 iterations, resulting in spectral filters with 10 μm size for each spatial point. The BMSFA consists of filtering units that arrange the spectral filters in a 4×4 configuration. This structure encodes the spatial-spectral data cube into two-dimensional measurement, which is then recovered using our proposed reconstruction algorithm. Experimental results demonstrate the superiorities of our sensor on spatial-spectral-temporal resolution, spectral detection range, light throughput, and signal-to-noise ratio. Meanwhile, we demonstrate the versatility, flexibility, and robustness of our sensor in applications such as agricultural monitoring, human health, and face anti-spoofing.

Based on the present work, we could optimize the framework in terms of materials, manufacturing techniques, algorithms, and scalability to improve

its overall capability. The performance of the sensor could be significantly affected by both the properties and quantity of spectral modulation materials employed. Specifically, we could improve the spectral perception capabilities of the sensor by exploring material combinations with a broader spectral response range. This creates a quasi-orthogonal space during the sampling and data compression process. Numerous studies have demonstrated the exceptional optical properties of 2D materials [27, 28], such as black phosphorus [29, 30], hexagonal boron nitride [31], graphene [32], transition metal dichalcogenides [33], and 2D superlattices [34, 35], which make them suitable for spectral modulation.

However, the precision of fabricating BMSFA decreases with an increase in the number of materials or a reduction in the structure size. To obtain high-precision BMSFA, it is necessary to improve the processing precision using advanced processing techniques, such as laser lithography [36–38], electron-beam lithography [39], imprint lithography [40], plasmonic lithography [41].

The large spatial resolution of the filter arrays presents a significant challenge for high-precision and high-resolution hyperspectral image reconstruction, especially when the sensor is applied on mobile platforms. It is crucial to make a tradeoff between platform resources and reconstruction performances. Therefore, lightweight networks that compress model parameters and reduce computational costs are preferred in such cases [42]. Currently, most hyperspectral image reconstruction models do not account for the effect of light sources. However, different lighting conditions can significantly impact the performance and generalization of these models. One approach to address this issue is to employ techniques such as tensor decomposition. [43] to simultaneously reconstruct the light source spectrum and spectral reflectance. We can customize sensors for specific applications, which can further improve their applicability. For instance, selecting spectral modulation materials carefully and focusing on reconstructing specific spectral bands can maximize the acquisition of spectral information in the characteristic wavelength bands. This approach not only enables computing speed and optimizes resource allocation by selectively reconstructing the spectral information of feature-point regions, but it also eliminates the need for reconstructing the entire hyperspectral image in certain tasks. Furthermore, in some cases, it is even not necessary to perform hyperspectral image reconstruction. Instead, we can directly analyze semantic information from the acquired data using an end-to-end analysis approach, bypassing the reconstruction step entirely. [44].

With the continuous advancements in materials, image sensors, precision optical instruments, and other related technologies, our framework has the potential to leverage these developments and incorporate new optimization strategies to enhance its performance. Existing on-chip hyperspectral imaging sensors, such as Photonic crystal slabs, Fabry-Pérot interferometers, Meta-surfaces, and others, typically involve the independent design of the spectral modulation structure and the image sensor, followed by their integration.

However, this manufacturing process introduces optical crosstalk, which hinders further improvements in spectral and spatial resolution. To address these limitations, the development of organic photodiodes (OPDs) offers a viable solution. OPDs have unique optical properties achieved through the doping of semiconductor materials with specific organic substances. This research field has gained significant attention, focusing on applications such as full-color detection, image sensing, and narrow-band spectral detection [45–48]. Physically and directly modulating the spectral properties of organic photodiodes provides a new idea for the design of integrated spectral imaging systems [49, 50]. Therefore, we can set up an imaging array using various OPDs to create a miniature imaging spectrometer.

Focus on the expansion of the imaging band, the framework of the HyperspecI sensor can be migrated to the middle infrared (MIR) range, even to the far infrared (FIR) range. BMSFA is a vital component that affects the working band and application of spectral cameras. Existing material systems, such as metal oxides and azo dyes [51], have a modulation effect of light in middle and far infrared bands. These materials can be used to fabricate BMSFA by photolithography. The multi-layer film [52] with a different refractive index covering a substrate can realize good filtering performance and be a BMSFA for middle and far infrared bands. Micro-hole multispectral filter [53], which is a micro-hole array constructed on precious metal layers by micro-etching, has the same functions as the BMSFA. Its transmission peaks can be continuously tuned from 3 μ m to 14 μ m. Fabry-Pérot cavity [54] can also achieve the functions of the BMSFA by the surface waveguide and the voltage acting on the cavity. Infrared imaging plays an important role in the detection of day, night, rain, and fog, which breaks through human visual impairment to realize anti-interference, strong target recognition, and all-weather work.

Regarding uncertainties induced by the complicated environment, HyperspecI could be further integrated with other sensors (such as LIDAR and SAR) to establish multi-source data fusion [55]. Those fusions contribute to overcoming the capability limitations on individual sensors' spatial and temporal resolution subsequently, and facilitate the reliable decision of an intelligent system. Specifically, for the case of interference scenarios, uncertainty representation via multi-source data fusion could improve the mapping relationship accuracy between spectra and objects [56]. Moreover, the sub-pixel level small target identification could be achieved via the fusion algorithm, for example, each pixel's data decoupling with underdetermined observations. Given the high-dimensional and multi-scale information from diverse sources, investigations on lightweight fusion algorithms are also essential for online information processing and intelligent decision-making in high-risk real-world applications, such as satellites and autonomous vehicles [57].

Fundamentally, the performance of an imaging system is largely confined by the physical limitations of its optical elements. The HyperspecI sensor could be employed to replace conventional cameras in other imaging platforms, thus

realizing higher-dimensional and multi-functional sensing for various applications. For example, integrating a vibrating coded microlens array to our sensor could achieve high-speed aberration-corrected 3D photography with spectral information [58]. Combining with ultra-fast imaging technology could achieve high-speed spectral imaging detection, which is suitable for capturing transient scenes [59] like explosive combustion science. Furthermore, when combined with a polarization imaging sensor, the HyperspecI sensor can provide detailed information about both the spectral and polarization properties of a scene. Polarization imaging captures the polarization state of light, which can provide information about the surface properties of objects such as their shape, roughness, and material composition [60]. Additionally, combined with the fluorescence imaging system, fluorescence signals could be effectively separated based on spectral features, thus improving the detection sensitivity of target tissues [61]. Moreover, miniaturized sensor shows tremendous potential for integration into portable devices such as smartphones or drones, which could enable new applications in fields such as environmental monitoring, precision agriculture, and human health. However, the feasibility of such systems would depend on many factors such as component design and integration. Further research and development are necessary to determine the practicality and viability of these systems.

Inter-pixel crosstalk poses limitations on pixel size reduction and spatial resolution improvement in image sensors. One of the main factors constraining the imaging performance of narrow-band multispectral cameras and RGB cameras is spectral crosstalk, which needs each pixel to have a unique spectral response and is susceptible to interference from neighboring pixels. However, HyperspecI sensor employs broadband modulation materials and computational reconstruction methods to acquire spectral information, eliminating the demand for strict consistency in spectral responses among pixels. Moreover, we utilize spectral calibration methods to obtain the response of each pixel, avoiding the influence of spectral crosstalk. Additionally, the integration of our HyperspecI sensor through photolithography mitigates optical crosstalk arising from interference or diffraction.

Tab 1: Comparison of different snapshot hyperspectral imaging technologies

| Abbr | Filter structure | Integration type | Spatial resolution (pixels) | Spectral resolution (bands/nm) | Response range (nm) | Year | Ref. |
|-------------|--------------------------------------|------------------|-----------------------------|--------------------------------|----------------------------|-------------|----------|
| CTIS | Grating | system | 11×11 | 20 / - | 300 (470-770) | 1995 | [11] |
| SD-CASSI | Coded aperture + prism | system | 128×128 | 28 / - | 100 (540-640) | 2008 | [12] |
| PMVIS | | system | 50×44 | 100 / 6 | 600 (400-1000) | 2011 | [13] |
| - | Photonic crystal slabs | on chip | 10×10 | - / 1 | 200 (550-750) | 2019 | [19] |
| - | | | - | 70 / 1.5 | 100 (750-850) | 2019 | [17] |
| MMSI | Metasurfaces | on chip | 290×200 | 20 / 7 | 185 (795-980) | 2020 | [62] |
| RTSI CIS | | | 356×436 | - / 0.8 | 300 (450-750) | 2022 | [18] |
| - | Scattering medium narrow-band filter | + on chip | 448×320 | 64 / - | 512 (386-898) | 2020 | [23] |
| - | Fabry-Pérot (narrow-band filter) | on chip | - | 8 / - | 300 (400-700) | 2019 | [63] |
| - | Fabry-Pérot (broadband filter) | on chip | 1920×1080 | 20 / 10 | 200 (450-750) | 2023 | [20] |
| THETA | Color film | on chip | 7000×9344 | 12 / - | 279 (406-684) | 2023 | [64] |
| Ours | Broadband material | on chip | 2048×2048 | 89 / 2.65 | 1300 (400-1700) | 2023 | - |

Acknowledgements This work was supported by the National Natural Science Foundation of China (61971045, 61827901, 62131003, 61991451).

Author contributions L.B., Z.W. and Y.Z.Z. designed the project. Z.W. and Y.Z.Z. designed and built the optical filter arrays. Y.Z.Z. and Y.N.Z. designed and implemented sensor integration. Y.Z.Z. and D.Z. designed the mechanical system. Z.W., C.Y., and W.F. conducted material optical performance tests and material preparation. Z.W. and C.Z. developed the overall pipeline of the reconstruction algorithms and conducted the simulation experiment. Z.W. and Y.Z.Z. designed the experiment scheme and tested the performance of the sensor. L.L. and Y.N.Z. designed and implemented the experiments of chlorophyll and SSC detection. Y.Z.Z. and Y.N.Z. conducted blood oxygen and water quality monitoring experiments. Y.Z.Z. and J.J.Z. conducted the anti-spoofing face recognition experiment. L.B. and J.Z. supervised the work. L.B., Z.W., Y.Z.Z., Y.N.Z., C.Y., L.L., and J.Z. prepared the

figures and wrote the manuscript with input from all authors.

Competing interests L.B., Y.Z.Z, Z.W., and J.Z. hold patents on technologies related to the devices developed in this work (China patent numbers ZL 2022 1 0764143.4, ZL 2022 1 0764143.4, ZL 2022 1 0764141.5, ZL 2019 1 0441784.4, ZL 2019 1 0482098.1 and ZL 2019 1 1234638.0) submitted related patent applications.

References

- [1] Landgrebe, D.: Hyperspectral image data analysis. *IEEE Signal Proc. Mag.* **19**(1), 17–28 (2002)
- [2] Yang, Z., Albrow-Owen, T., Cui, H., Alexander-Webber, J., Gu, F., Wang, X., Wu, T.-C., Zhuge, M., Williams, C., Wang, P., *et al.*: Single-nanowire spectrometers. *Science* **365**(6457), 1017–1020 (2019)
- [3] Li, S., Song, W., Fang, L., Chen, Y., Ghamisi, P., Benediktsson, J.A.: Deep learning for hyperspectral image classification: An overview. *IEEE T. Geosci. Remote* **57**(9), 6690–6709 (2019)
- [4] Backman, V., Wallace, M.B., Perelman, L., Arendt, J., Gurjar, R., Müller, M., Zhang, Q., Zonios, G., Kline, E., McGillican, T., *et al.*: Detection of preinvasive cancer cells. *Nature* **406**(6791), 35–36 (2000)
- [5] Dremin, V., Marcinkevics, Z., Zherebtsov, E., Popov, A., Grabovskis, A., Kronberga, H., Geldnere, K., Doronin, A., Meglinski, I., Bykov, A.: Skin complications of diabetes mellitus revealed by polarized hyperspectral imaging and machine learning. *IEEE T. Med. Imaging* **40**(4), 1207–1216 (2021)
- [6] Hadoux, X., Hui, F., Lim, J.K., Masters, C.L., Pébay, A., Chevalier, S., Ha, J., Loi, S., Fowler, C.J., Rowe, C., *et al.*: Non-invasive in vivo hyperspectral imaging of the retina for potential biomarker use in Alzheimer’s disease. *Nat. Commun.* **10**(1), 4227 (2019)
- [7] Mehl, P.M., Chen, Y.-R., Kim, M.S., Chan, D.E.: Development of hyperspectral imaging technique for the detection of apple surface defects and contaminations. *J. Food Eng.* **61**(1), 67–81 (2004)
- [8] Rao, S., Huang, Y., Cui, K., Li, Y.: Anti-spoofing face recognition using a metasurface-based snapshot hyperspectral image sensor. *Optica* **9**(11), 1253–1259 (2022)
- [9] Green, R.O., Eastwood, M.L., Sarture, C.M., Chrien, T.G., Aronsson, M., Chippendale, B.J., Faust, J.A., Pavri, B.E., Chovit, C.J., Solis, M., *et al.*: Imaging spectroscopy and the airborne visible/infrared imaging spectrometer (AVIRIS). *Remote Sens. Environ.* **65**(3), 227–248 (1998)
- [10] Pian, Q., Yao, R., Sinsuebphon, N., Intes, X.: Compressive hyperspectral time-resolved wide-field fluorescence lifetime imaging. *Nat. photonics* **11**(7), 411–414 (2017)
- [11] Descour, M., Dereniak, E.: Computed-tomography imaging spectrometer: experimental calibration and reconstruction results. *Appl. Optics* **34**(22),

4817–4826 (1995)

- [12] Wagadarikar, A., John, R., Willett, R., Brady, D.: Single disperser design for coded aperture snapshot spectral imaging. *Appl. Optics* **47**(10), 44–51 (2008)
- [13] Cao, X., Du, H., Tong, X., Dai, Q., Lin, S.: A prism-mask system for multispectral video acquisition. *IEEE T. Pattern Anal.* **33**(12), 2423–2435 (2011)
- [14] Arguello, H., Arce, G.R.: Colored coded aperture design by concentration of measure in compressive spectral imaging. *IEEE T. Image Process.* **23**(4), 1896–1908 (2014)
- [15] Geelen, B., Tack, N., Lambrechts, A.: A compact snapshot multispectral imager with a monolithically integrated per-pixel filter mosaic. In: *Advanced Fabrication Technologies for Micro/nano Optics and Photonics VII*, vol. 8974, pp. 80–87 (2014)
- [16] Yesilkoy, F., Arvelo, E.R., Jahani, Y., Liu, M., Tittl, A., Cevher, V., Kivshar, Y., Altug, H.: Ultrasensitive hyperspectral imaging and biodection enabled by dielectric metasurfaces. *Nat. Photonics* **13**(6), 390–396 (2019)
- [17] Faraji-Dana, M., Arbabi, E., Kwon, H., Kamali, S.M., Arbabi, A., Bartholomew, J.G., Faraon, A.: Hyperspectral imager with folded metasurface optics. *ACS Photonics* **6**(8), 2161–2167 (2019)
- [18] Xiong, J., Cai, X., Cui, K., Huang, Y., Yang, J., Zhu, H., Li, W., Hong, B., Rao, S., Zheng, Z., *et al.*: Dynamic brain spectrum acquired by a real-time ultraspectral imaging chip with reconfigurable metasurfaces. *Optica* **9**(5), 461–468 (2022)
- [19] Wang, Z., Yi, S., Chen, A., Zhou, M., Luk, T.S., James, A., Nogan, J., Ross, W., Joe, G., Shahsafi, A., *et al.*: Single-shot on-chip spectral sensors based on photonic crystal slabs. *Nat. Commun.* **10**(1), 1020 (2019)
- [20] Yako, M., Yamaoka, Y., Kiyohara, T., Hosokawa, C., Noda, A., Tack, K., Spooren, N., Hirasawa, T., Ishikawa, A.: Video-rate hyperspectral camera based on a cmos-compatible random array of fabry–pérot filters. *Nat. Photonics* **17**(3), 218–223 (2023)
- [21] Bao, J., Bawendi, M.G.: A colloidal quantum dot spectrometer. *Nature* **523**(7558), 67–70 (2015)
- [22] Zhu, X., Bian, L., Fu, H., Wang, L., Zou, B., Dai, Q., Zhang, J., Zhong, H.: Broadband perovskite quantum dot spectrometer beyond human visual

- resolution. *Light: Sci. Appl.* **9**(1), 73 (2020)
- [23] Monakhova, K., Yanny, K., Aggarwal, N., Waller, L.: Spectral diffusercam: lensless snapshot hyperspectral imaging with a spectral filter array. *Optica* **7**(10), 1298–1307 (2020)
- [24] Redding, B., Liew, S.F., Sarma, R., Cao, H.: Compact spectrometer based on a disordered photonic chip. *Nat. Photonics* **7**(9), 746–751 (2013)
- [25] Limantara, L., Dettling, M., Indrawati, R., Brotosudarmo, T.H.P., *et al.*: Analysis on the chlorophyll content of commercial green leafy vegetables. *Procedia Chem.* **14**, 225–231 (2015)
- [26] Gitelson, A.A., Merzlyak, M.N., Lichtenthaler, H.K.: Detection of red edge position and chlorophyll content by reflectance measurements near 700 nm. *J. plant physiol.* **148**(3-4), 501–508 (1996)
- [27] Yu, S., Wu, X., Wang, Y., Guo, X., Tong, L.: 2d materials for optical modulation: challenges and opportunities. *Adv. Mater.* **29**(14), 1606128 (2017)
- [28] Xia, F., Wang, H., Xiao, D., Dubey, M., Ramasubramaniam, A.: Two-dimensional material nanophotonics. *Nat. Photonics* **8**(12), 899–907 (2014)
- [29] Yuan, S., Naveh, D., Watanabe, K., Taniguchi, T., Xia, F.: A wavelength-scale black phosphorus spectrometer. *Nat. Photonics* **15**(8), 601–607 (2021)
- [30] Kim, H., Uddin, S.Z., Lien, D.-H., Yeh, M., Azar, N.S., Balendhran, S., Kim, T., Gupta, N., Rho, Y., Grigoropoulos, C.P., *et al.*: Actively variable-spectrum optoelectronics with black phosphorus. *Nature* **596**(7871), 232–237 (2021)
- [31] Chugh, D., Jagadish, C., Tan, H.: Large-area hexagonal boron nitride for surface enhanced raman spectroscopy. *Adv. Mater. Technologies* **4**(8), 1900220 (2019)
- [32] Koppens, F., Mueller, T., Avouris, P., Ferrari, A., Vitiello, M., Polini, M.: Photodetectors based on graphene, other two-dimensional materials and hybrid systems. *Nat. Nanotechnol.* **9**(10), 780–793 (2014)
- [33] Geng, D., Yang, H.Y.: Recent advances in growth of novel 2D materials: beyond graphene and transition metal dichalcogenides. *Adv. Mater.* **30**(45), 1800865 (2018)
- [34] Zhou, J., Zhang, W., Lin, Y.-C., Cao, J., Zhou, Y., Jiang, W., Du, H.,

- Tang, B., Shi, J., Jiang, B., *et al.*: Heterodimensional superlattice with in-plane anomalous hall effect. *Nature* **609**(7925), 46–51 (2022)
- [35] Wang, C., He, Q., Halim, U., Liu, Y., Zhu, E., Lin, Z., Xiao, H., Duan, X., Feng, Z., Cheng, R., *et al.*: Monolayer atomic crystal molecular superlattices. *Nature* **555**(7695), 231–236 (2018)
- [36] Ito, T., Okazaki, S.: Pushing the limits of lithography. *Nature* **406**(6799), 1027–1031 (2000)
- [37] Huang, L., Xu, K., Yuan, D., Hu, J., Wang, X., Xu, S.: Sub-wavelength patterned pulse laser lithography for efficient fabrication of large-area metasurfaces. *Nat. Commun.* **13**(1), 5823 (2022)
- [38] Öktem, B., Pavlov, I., Ilday, S., Kalaycıoğlu, H., Rybak, A., Yavaş, S., Erdoğan, M., Ilday, F.Ö.: Nonlinear laser lithography for indefinitely large-area nanostructuring with femtosecond pulses. *Nat. Photonics* **7**(11), 897–901 (2013)
- [39] Kim, S., Marelli, B., Brenckle, M.A., Mitropoulos, A.N., Gil, E.-S., Tsioris, K., Tao, H., Kaplan, D.L., Omenetto, F.G.: All-water-based electron-beam lithography using silk as a resist. *Nat. Nanotechnol.* **9**(4), 306–310 (2014)
- [40] Gan, Z., Feng, H., Chen, L., Min, S., Liang, C., Xu, M., Jiang, Z., Sun, Z., Sun, C., Cui, D., *et al.*: Spatial modulation of nanopattern dimensions by combining interference lithography and grayscale-patterned secondary exposure. *Light: Sci. Appl.* **11**(1), 89 (2022)
- [41] Han, D., Deng, S., Ye, T., Wei, Y.: Enhancement of pattern quality in maskless plasmonic lithography via spatial loss modulation. *Microsyst. Nanoeng.* **9**(1), 40 (2023)
- [42] Yu, C., Xiao, B., Gao, C., Yuan, L., Zhang, L., Sang, N., Wang, J.: Lite-hrnet: A lightweight high-resolution network. In: *Proceedings of the IEEE/CVF Conference on Computer Vision and Pattern Recognition*, pp. 10440–10450 (2021)
- [43] Zheng, Y., Sato, I., Sato, Y.: Illumination and reflectance spectra separation of a hyperspectral image meets low-rank matrix factorization. In: *Proceedings of the IEEE Conference on Computer Vision and Pattern Recognition*, pp. 1779–1787 (2015)
- [44] Peng, L., Xie, S., Qin, T., Cao, L., Bian, L.: Image-free single-pixel object detection. *Opt. Lett.* **48**(10), 2527–2530 (2023)
- [45] Fuentes-Hernandez, C., Chou, W.-F., Khan, T.M., Diniz, L., Lukens,

- J., Larrain, F.A., Rodriguez-Toro, V.A., Kippelen, B.: Large-area low-noise flexible organic photodiodes for detecting faint visible light. *Science* **370**(6517), 698–701 (2020)
- [46] Jansen-van Vuuren, R.D., Armin, A., Pandey, A.K., Burn, P.L., Meredith, P.: Organic photodiodes: the future of full color detection and image sensing. *Adv. Mater.* **28**(24), 4766–4802 (2016)
- [47] Labanti, C., Wu, J., Shin, J., Limbu, S., Yun, S., Fang, F., Park, S.Y., Heo, C.-J., Lim, Y., Choi, T., *et al.*: Light-intensity-dependent photoresponse time of organic photodetectors and its molecular origin. *Nat. Commun.* **13**(1), 3745 (2022)
- [48] Lim, Y., Yun, S., Minami, D., Choi, T., Choi, H., Shin, J., Heo, C.-J., Leem, D.-S., Yagi, T., Park, K.-B., *et al.*: Green-light-selective organic photodiodes with high detectivity for cmos color image sensors. *ACS Appl. Mater. Inter.* **12**(46), 51688–51698 (2020)
- [49] Armin, A., Jansen-van Vuuren, R.D., Kopidakis, N., Burn, P.L., Meredith, P.: Narrowband light detection via internal quantum efficiency manipulation of organic photodiodes. *Nat. Commun.* **6**(1), 6343 (2015)
- [50] Wang, Y., Siegmund, B., Tang, Z., Ma, Z., Kublitski, J., Xing, S., Nikolis, V.C., Ullbrich, S., Li, Y., Benduhn, J., *et al.*: Stacked dual-wavelength near-infrared organic photodetectors. *Adv. Opt. Mater.* **9**(6), 2001784 (2021)
- [51] Ahmed, F., Dewani, R., Pervez, M., Mahboob, S., Soomro, S.: Non-destructive ft-ir analysis of mono azo dyes. *Bulg. Chem. Commun* **48**(1), 71–77 (2016)
- [52] Wolf, O., Campione, S., Benz, A., Ravikumar, A.P., Liu, S., Luk, T.S., Kadlec, E.A., Shaner, E.A., Klem, J.F., Sinclair, M.B., *et al.*: Phased-array sources based on nonlinear metamaterial nanocavities. *Nat. Commun.* **6**(1), 7667 (2015)
- [53] Wang, A., Dan, Y.: Mid-infrared plasmonic multispectral filters. *Sci. Rep.* **8**(1), 11257 (2018)
- [54] Wang, X., Chen, C., Pan, L., Wang, J.: A graphene-based fabry-pérot spectrometer in mid-infrared region. *Sci. Rep.* **6**(1), 1–10 (2016)
- [55] Abdar, M., Pourpanah, F., Hussain, S., Rezazadegan, D., Liu, L., Ghavamzadeh, M., Fieguth, P., Cao, X., Khosravi, A., Acharya, U.R., *et al.*: A review of uncertainty quantification in deep learning: Techniques, applications and challenges. *Inf. Fusion* **76**, 243–297 (2021)

- [56] Hénaff, O.J., Boundy-Singer, Z.M., Meding, K., Ziemba, C.M., Goris, R.L.: Representation of visual uncertainty through neural gain variability. *Nat. Commun.* **11**(1), 2513 (2020)
- [57] Almalioglu, Y., Turan, M.h., Trigoni, N., Markham, A.: Deep learning-based robust positioning for all-weather autonomous driving. *Nat. Mach. Intell.* **4**(9), 749–760 (2022)
- [58] Wu, J., Guo, Y., Deng, C., Zhang, A., Qiao, H., Lu, Z., Xie, J., Fang, L., Dai, Q.: An integrated imaging sensor for aberration-corrected 3D photography. *Nature*, 62–71 (2022)
- [59] Gao, L., Liang, J., Li, C., Wang, L.V.: Single-shot compressed ultrafast photography at one hundred billion frames per second. *Nature* **516**(7529), 74–77 (2014)
- [60] Altaqui, A., Sen, P., Schrickx, H., Rech, J., Lee, J.-W., Escuti, M., You, W., Kim, B.J., Kolbas, R., O’Connor, B.T., *et al.*: Mantis shrimp-inspired organic photodetector for simultaneous hyperspectral and polarimetric imaging. *Sci. Adv* **7**(10), 3196 (2021)
- [61] Shi, W., Koo, D.E., Kitano, M., Chiang, H.J., Trinh, L.A., Turcatel, G., Steventon, B., Arnesano, C., Warburton, D., Fraser, S.E., *et al.*: Pre-processing visualization of hyperspectral fluorescent data with spectrally encoded enhanced representations. *Nat. Commun.* **11**(1), 726 (2020)
- [62] McClung, A., Samudrala, S., Torfeh, M., Mansouree, M., Arbabi, A.: Snapshot spectral imaging with parallel metasystems. *Sci. Adv.* **6**(38), 7646 (2020)
- [63] Williams, C., Gordon, G.S., Wilkinson, T.D., Bohndiek, S.E.: Grayscale-to-color: scalable fabrication of custom multispectral filter arrays. *ACS Photonics* **6**(12), 3132–3141 (2019)
- [64] Zhang, W., Dong, K., Li, L., Yuan, X., Pei, C., Suo, J., Dai, Q.: Handheld snapshot multi-spectral camera at 65-megapixel resolution (2023)